

Tunable ultrasharp terahertz plasma edge in a lightly doped narrow-gap semiconductor

XUEWEI JU,¹ ZHIQIANG HU,¹ FENG HUANG,¹ HAIBIN WU,¹ ALEXEY BELYANIN,² JUNICHIRO KONO,^{3,4,5} AND XIANGFENG WANG^{1,*}

¹School of Mechanical Engineering and Automation, Fuzhou University, Fuzhou, 350108, China

²Department of Physics, Texas A&M University, College Station, Texas 77843, USA

³Department of Electrical and Computer Engineering, Rice University, Houston, Texas 77005, USA

⁴Department of Physics and Astronomy, Rice University, Houston, Texas 77005, USA

⁵Department of Materials Science and NanoEngineering, Rice University, Houston, Texas 77005, USA

*xfwang@fzu.edu.cn

Abstract: Plasma edges in metals typically occur in the visible range, producing characteristic colors of metals. In a lightly doped semiconductor, the plasma edge can occur in the terahertz (THz) frequency range. Due to low scattering rates and variable electron densities in semiconductors, such THz plasma edges can be extremely sharp and greatly tunable. Here, we show that an ultrasharp THz plasma edge exists in a lightly *n*-doped InSb crystal with a record-high transmittance slope of 80 dB/THz. The frequency at which this sharp edge happens can be readily tuned by changing the temperature, electron density, scattering rate, and sample thickness. The edge frequency exhibited a surprising increase with decreasing temperature below 15 K, which we explain as a result of a weak-to-strong transition in the scattering rate, going from $\omega\tau \gg 1$ to $\omega\tau \sim 1$. These results indicate that doped narrow-gap semiconductors provide a versatile platform for manipulating THz waves in a controllable manner, especially as a high-pass filter with an unprecedented on/off ratio.

© 2021 Optical Society of America under the terms of the [OSA Open Access Publishing Agreement](#)

1. Introduction

A characteristic frequency at which the material changes from a metallic to a dielectric response is called the plasma frequency ω_p , which is defined as the frequency at which the real part of the dielectric function vanishes [1]. According to Drude theory, the dielectric function in the long-wavelength limit of a material containing free electrons can be written as

$$\tilde{\epsilon}(\omega) = \epsilon_1(\omega) + i\epsilon_2(\omega) = \left(\kappa_l - \frac{ne^2}{\epsilon_0 m^* (\nu^2 + \omega^2)} \right) + i \left(\frac{ne^2 \nu}{\epsilon_0 m^* \omega (\nu^2 + \omega^2)} \right), \quad (1)$$

where $\epsilon_1(\omega)$ and $\epsilon_2(\omega)$ are the real and imaginary parts of the dielectric function, respectively, n is the free electron density, e is the electron charge, ϵ_0 is the vacuum permittivity, κ_l is the lattice dielectric constant, m^* is the effective mass of the electrons, ν is the electron scattering rate, and ω is the angular frequency. $\epsilon_1(\omega)$ vanishes when

$$\kappa_l - \frac{ne^2}{\epsilon_0 m^* (\nu^2 + \omega^2)} = 0. \quad (2)$$

The solution to this equation yields the bulk plasmon resonance frequency:

$$\omega_r = \sqrt{\frac{ne^2}{\epsilon_0 \kappa_l m^*} - \nu^2}. \quad (3)$$

This frequency is usually identified as the low-frequency cutoff in electromagnetic wave propagation through a bulk plasma. For semiconductors at frequencies above the optical phonon

frequencies, it is usually true that $\omega\tau \gg 1$ ($\tau = 1/\nu$, is the relaxation time). Thus, it is customary to neglect the scattering rate ν in Eq. (3) and approximate ω_r by the plasma frequency defined as

$$\omega_p = \sqrt{\frac{ne^2}{\epsilon_0\kappa/m^*}}. \quad (4)$$

Free electrons in the conduction band of a doped narrow-gap semiconductor, such as InSb and HgCdTe, respond to a low-frequency ac field as a classical solid-state plasma as long as interband transitions can be neglected. Owing to the low electron densities (compared to metals), small effective masses, and high mobilities in these materials, most of the relevant energy scales (e.g., the plasma energy, the Fermi energy, and the donor binding energy) fall into the meV energy range, creating a fertile playground for exploring novel terahertz (THz) physics and applications (1 THz is equivalent to 4.1 meV). A variety of interesting phenomena have been observed in these systems, including interference-induced transparency [2], giant Faraday rotation [3], magnetoquantum oscillations [4], the Voigt effect [5], photonic Weyl points [6], magneto-optical Kerr effect [7], and metal-to-insulator transitions [8].

Here, we used time-domain THz spectroscopy to investigate a lightly *n*-doped InSb crystal at different temperatures from 1.6 to 250 K. We observed an ultrasharp plasma edge with a record-high transmittance slope of 80 dB/THz. We found that the edge frequency, defined as the transmission cutoff frequency ω_c , is highly tunable, sensitively varying with the temperature, electron density, scattering rate, and sample thickness. In particular, ω_c exhibited a sudden increase with decreasing temperature at around 15 K. To explain this surprising phenomenon, we developed a theoretical model of THz transmission through the sample, which takes into account the temperature dependence of the electron density, scattering rate, bandgap, and effective mass. Through detailed comparison between experiment and theory, we concluded that the electron scattering rate experiences a weak-to-strong transition (from $\omega\tau \gg 1$ to $\omega\tau \sim 1$) as the temperature goes below 15 K. The resulting increase in absorption losses causes an observed increase in the low-frequency cutoff in the transmission spectrum, despite the decrease of ω_r and ω_p with decreasing temperature. These results demonstrate that doped narrow-gap semiconductors provide a high-pass filter for manipulating THz waves in a highly controllable manner.

2. Experimental methods

The pump source in our time-domain THz spectroscopy system was a femtosecond amplified Ti:sapphire laser (Astrella, Coherent, Inc.) with a wavelength of 800 nm, a pulse width of 35 fs, a repetition rate of 1 kHz, and a pulse energy of 5 mJ [9]. We used a pair of <110> ZnTe crystals to generate and detect coherent THz radiation with frequency components from 0.1 to 2.5 THz through surface rectification and electro-optic sampling, respectively [10]. The sample was mounted in a cryogen-free cryostat (SpectromagPT, Oxford Instruments, Inc.), and the sample temperature was varied from 1.6 to 300 K. We used a standard lock-in scheme for time-domain signal detection.

The sample studied was a large ($\sim 0.8 \times 20 \times 30$ mm³) crystal of Te-doped *n*-InSb with an electron density of 2.3×10^{14} cm⁻³ and a 2 K mobility of 7.7×10^4 cm² V⁻¹ s⁻¹. The Fermi energy was 0.9 meV (or 0.21 THz), and $\omega_p \approx 2\pi \times 0.3$ THz at 40 K. A linearly polarized THz wave was normally incident onto the sample surface, and we measured the waveforms of the transmitted THz wave at a set of fixed temperatures. We also measured THz waveforms transmitted through an empty hole as a reference. Then we Fourier-transformed the time-domain waveforms into the frequency domain and normalized the power spectra to obtain transmittance spectra. To eliminate interference fringes owing to multiple reflections within the sample, only the transmittance spectra of the first pulse that goes directly through the sample were used in all

figures. In order to eliminate the influence of water vapor absorption on the spectrum, the THz system was fully sealed and filled with dry nitrogen.

3. Results and discussion

Figure 1(a) shows experimental and calculated transmittance spectra for the InSb sample at 1.6 K and 40 K. A very sharp edge is seen in the transmittance spectra. The transmittance is plotted in dB, and the 30 dB attenuation point (a residual transmission power of 0.1%) is extracted as the low-frequency cutoff, ω_c . Figure 1(b) plots the value of ω_c measured at different temperatures, including those obtained through our developed full theory that takes propagation effects into account and the plasmon resonance frequency based on Eqs. (3) and (4). One can see that ω_c increases when the temperature decreases below 15 K. This behavior is contradictory with the predicted decrease of ω_r and ω_p given by Eqs. (3) and (4), in which $\omega_p \propto \sqrt{n}$ and n usually decreases with decreasing temperature, whereas the electron scattering rate ν increases with decreasing temperature from 40 to 1.6 K, as our modeling shows below. This phenomenon can be directly seen in Fig. 1(a), where ω_c at 1.6 K is larger than that at 40 K. When the temperature is greater than 75 K, the value of ω_c extracted from the experiments also deviates from the values of ω_r and ω_p calculated using Eqs. (3) and (4), respectively, as shown in Fig. 1(b).

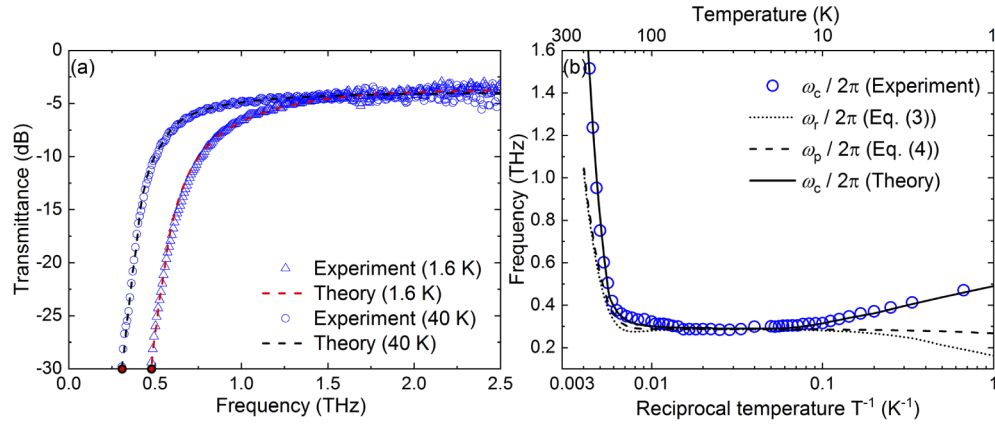


Fig. 1. (a) Experimental and calculated transmittance spectra of the n -InSb sample at 1.6 K and 40 K; (b) The transmission cutoff frequency $\omega_c/2\pi$, the bulk plasmon resonance frequency $\omega_r/2\pi$, and the plasma frequency $\omega_p/2\pi$ at different temperatures obtained from experiments, calculations of THz transmission, and Eqs. (3) and (4).

We developed a comprehensive theoretical model to calculate the temperature dependence of the effective mass (m^*), bandgap (E_g), electron density (n), and scattering rate (ν) of the n -InSb sample, where $m_0 = 9.11 \times 10^{-31}$ kg. The results are shown in Fig. 2. The electron density curve in Fig. 2(a) can be divided into three regions: the impurity ionization region (Region I, white), the saturation region (Region II, red), and the intrinsic excitation region (Region III, gray). At the lowest temperatures, all electrons are bound to impurity levels, but in Region I, an increasing portion of the electrons are thermally excited to the conduction band [11]. At around 15 K, essentially all electrons are in the conduction band, leaving all impurities ionized. Further increasing the temperature will not increase the electron density (Region II), since all donors are ionized and the free electron density is equal to the doping concentration in this region. In Region III, intrinsic thermal excitation across the bandgap occurs, resulting in an exponential growth of the electron density.

The scattering rate is determined by several microscopic processes over a temperature range from 1.6 to 250 K, including ionized and neutral impurity scattering, piezoelectric scattering,

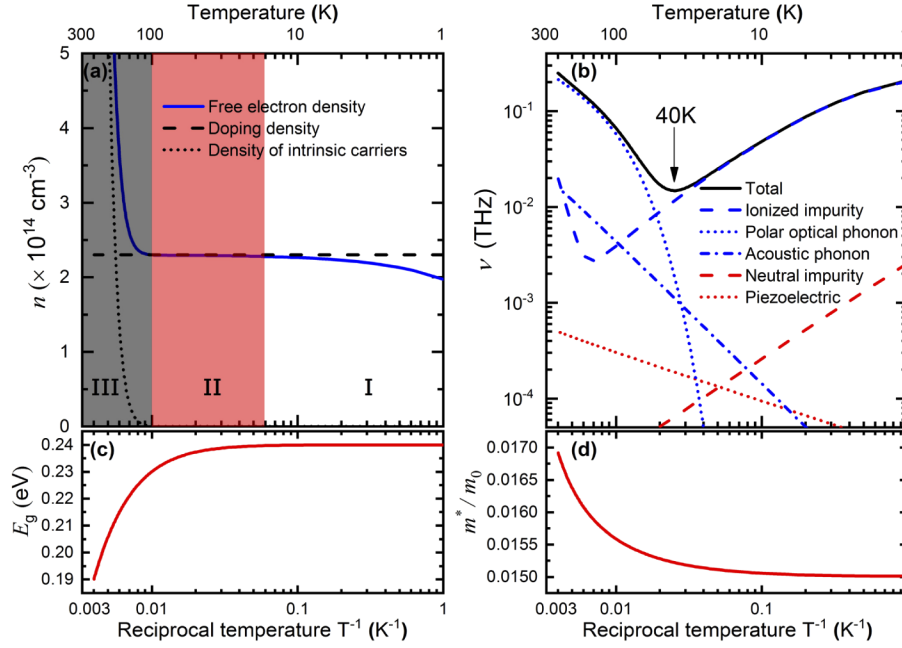


Fig. 2. Calculated temperature dependence of the (a) electron density n , (b) electron scattering rate ν , (c) band gap E_g , and (d) electron effective mass m^*/m_0 in an n-InSb sample.

and scattering by acoustic and polar optical phonons [2,12,13], exhibiting a nonmonotonic temperature dependence, see Fig. 2(b). At the lowest temperatures ($< \sim 15$ K), the dominant scatterers are neutral and ionized impurities, whereas at high temperatures ($> \sim 75$ K) the main scatterers are polar optical phonons. On the other hand, with increasing temperature, the bandgap E_g decreases and the effective mass m^* increases, as shown in Figs. 2(c) and 2(d).

The temperature dependence of the effective mass (m^*), bandgap (E_g), electron density (n), and scattering rate (ν) are calculated using the following equations [13–17]:

$$m^*(T) = \frac{0.015m_0}{1 - \frac{k_B T}{E_g}}, \quad (5)$$

$$E_g(T) = E_g(0) - \frac{\alpha T^2}{\beta + T}, \quad (6)$$

$$n(T) = n_e(T) + n_i(T), \quad (7)$$

$$n_e(T) \approx n_{\text{doped}} \cdot \exp(-E_{\text{bind}}/2k_B T), \quad (8)$$

$$n_i(T) \approx 1.1 \times 10^{14} T^{1.5} \exp(-E_g/2k_B T), \quad (9)$$

$$\nu_{\text{total}}(T) = \nu_1(T) + \nu_2(T) + \nu_3(T) + \nu_4(T) + \nu_5(T), \quad (10)$$

$$\nu_{1 \rightarrow 5} = \frac{e}{\mu_{1 \rightarrow 5} m^*}, \quad (11)$$

where $0.015m_0$ is the electron effective mass at the band edge, α and β are Varshni parameters [15], E_{bind} is the binding energy, $E_g(0)$ is the bandgap at 0 K, n_e and n_i are the doping and intrinsic electron densities under thermal excitation, respectively. Detailed expressions of all the mobility components ($\mu_1 - \mu_5$) representing different scattering processes (ionized and neutral impurity scattering, piezoelectric scattering, and scattering by acoustic and polar optical phonons)

are quite complicated and well documented in Ref. [13]. In addition, nonparabolicity of the conduction band is taken into account in Eq. (5), and we assume only a fraction of electrons ($\sim 1/4$) freezes out because of anti-site doping and partial overlap of impurity wave function at low temperatures in Eq. (8). A few important parameters are listed here, including $m^* = 0.015m_0$, $E_g(0) = 0.24$ eV, $E_{\text{bind}} = 0.75$ meV, $\alpha = 0.6$ meV/K, and $\beta = 500$ K. We substituted the calculated effective mass, bandgap, density, and scattering rate into Eq. (1) to obtain the real and imaginary parts of the permittivity at different temperatures.

The bulk n -InSb sample can be treated as a plane-parallel slab. The transmittance can be calculated by $T(\omega) = \tilde{T}_E(\omega)\tilde{T}_E(\omega)^*$, where $\tilde{T}_E(\omega)$ is the complex transmission coefficient of the THz electric field

$$\tilde{T}_E(\omega) = \frac{4\tilde{N}(\omega)}{(\tilde{N}(\omega) + 1)^2} \exp\{i(\tilde{N}(\omega) - 1)\omega d/c\}, \quad (12)$$

where d and c are the sample thickness and the velocity of light in vacuum, respectively. The complex refractive index, $\tilde{N}(\omega)$, is given by $\tilde{N}(\omega) = \sqrt{\tilde{\epsilon}(\omega)} = N(\omega) + iK(\omega)$. In the case of a thick sample, $K(\omega) \ll N(\omega)$ is common in semiconductors. Under these conditions, the power transmittance can be written as [18]

$$T(\omega) = \frac{\left[4\text{Re}\left(\sqrt{\tilde{\epsilon}(\omega)}\right)\right]^2}{\left(\text{Re}\left(\sqrt{\tilde{\epsilon}(\omega)}\right) + 1\right)^4} \exp\left\{-2\text{Im}\left(\sqrt{\tilde{\epsilon}(\omega)}\right)\omega d/c\right\}. \quad (13)$$

By finely tuning parameters in the above equations within a reasonable value range referring to the literature [13–17], we can achieve good agreement between experiment and theory as shown in Fig. 1.

The real and imaginary parts of the permittivity at different temperatures (1.6, 4, 10, 20, and 40 K) are shown in Figs. 3(a) and 3(b). According to the definition of the bulk plasmon resonance frequency, that is, the frequency at which the real part of the dielectric function vanishes, one can see that both the plasmon resonance frequency (ω_r) and the plasma frequency (ω_p) decrease with decreasing temperature, consistent with Eqs. (3) and (4), as well as the corresponding plots in Fig. 1(b). However, we notice that the imaginary part of the permittivity increases significantly at any given frequency with decreasing temperature. In the absence of a magnetic field, the attenuation and propagation constants, A and B in an isotropic sample are given by $A = \text{Im}\left(\sqrt{\tilde{\epsilon}(\omega)}\right)\omega/c$ and $B = \text{Re}\left(\sqrt{\tilde{\epsilon}(\omega)}\right)\omega/c$ [19]. This means that the absorption of the THz wave increases due to the increasing scattering rate (more collision loss), causing the transmission cutoff to move towards higher frequencies, which overcomes the decrease of the plasmon resonance frequency according to Eq. (3). The same explanation also applies to the anomalous increase of the transmission cutoff frequency (ω_c) above 75 K, because the scattering rate in the two temperature regions experiences a weak-to-strong transition (from $\omega\tau \gg 1$ to $\omega\tau \sim 1$). At 40 K and 0.3 THz (the plasmon resonance at 40 K), $\omega\tau$ equals ~ 120 , while it equals ~ 10 at 1.6 K and ~ 8 at 250 K. The value of ν or τ varies by more than 2 orders of magnitude. The strong scattering significantly modifies the absorption edges measured by THz transmission spectroscopy. According to the relationship $\tilde{\sigma}(\omega) = i(\kappa_l - \tilde{\epsilon}(\omega))\omega\epsilon_0 = \sigma_1(\omega) + i\sigma_2(\omega)$, the real and imaginary parts of the conductivity at different temperatures (1.6, 4, 10, 20, and 40 K) can be calculated, as shown in Figs. 3(c) and 3(d). The real part of the conductivity that represents absorption loss also increases with decreasing temperature at any given frequency within the THz pulse spectrum.

The calculated transmittance curves at 1.6 K and 40 K are shown in Fig. 1(a), which accurately reproduces the experimental results. In particular, the low-frequency transmission cutoffs ω_c at different temperatures obtained from experiments are well predicted by our developed theory, as shown in Fig. 1(b) (solid line). It should be noted that by fitting THz spectra using the

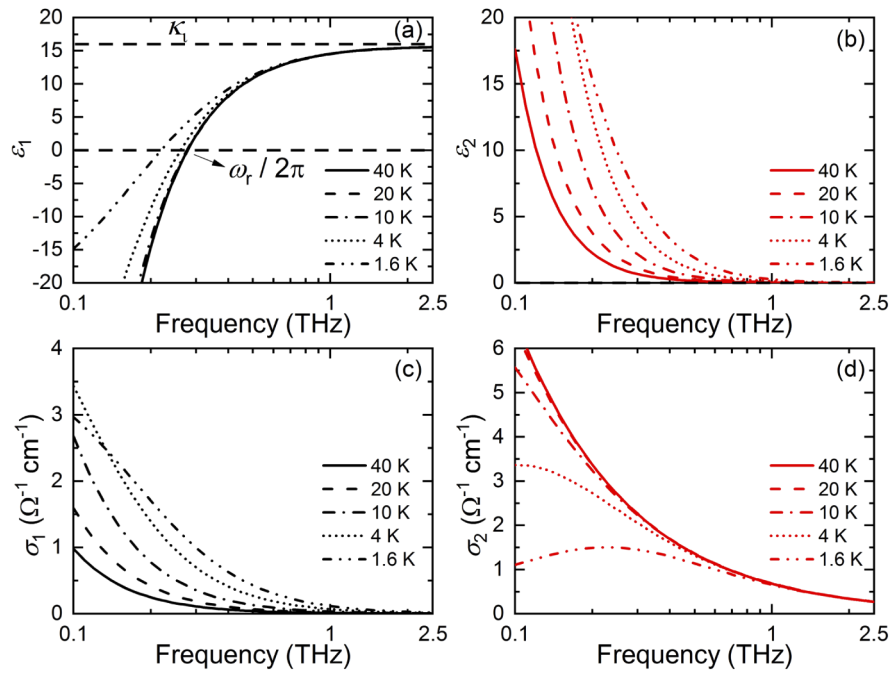


Fig. 3. The real (a) and imaginary (b) parts of the permittivity at temperatures of 1.6, 4, 10, 20, and 40 K. The frequency at which the real part of the permittivity vanishes is the bulk plasmon resonance frequency ($\omega_r/2\pi$). The real (c) and imaginary (d) parts of the conductivity at temperatures of 1.6, 4, 10, 20, and 40 K.

developed theory we could extract the electron density and mobility of the InSb sample at different temperatures, which are usually obtained by traditional four-contact transport measurements.

We can utilize the transmission characteristics of *n*-InSb to fabricate tunable high-pass THz filters. Due to the insertion loss, the maximal transmittance plateau is at -4 dB, as shown in Fig. 1(a). The transition steepness of the plasma edge can be defined by a slope factor $\xi = (\alpha_p - \alpha_c)/(f_p - f_c)$ [20], where α_p is the 7 dB-attenuation point, α_c is the 30 dB-attenuation point, and f_p and f_c are the frequencies at -7 dB and -30 dB, respectively. In Fig. 1(a), the factor ξ equals 80 dB/THz and 36 dB/THz at 40 K and 1.6 K respectively. To characterize the tunability and transition steepness, we plotted the filters' transmittance curves for different sample thicknesses, scattering rates, temperatures, and densities. The results and relevant parameters are shown in Figs. 4(a)–4(d). One can see that both the thickness and scattering rate alone affect the steepness of the plasma edge and modify the plasma frequency slightly. A significant absorption edge shift occurs through tuning either the doping density or temperature. The temperature affects not only the electron density but also the electron scattering rate, and thus, it can be used as a fine-tuning parameter. By using samples with different densities, the cutoff frequency can be broadly tuned from 0.21 THz to 4.1 THz, and the slope factor ξ can reach 290 dB/THz, 180 dB/THz, and 124 dB/THz for different doping densities (from left to right), respectively. THz high-pass filters have been proposed/fabricated based on parallel-plate waveguide, metamaterials and graphene, but they show poor tunability and slow transition edges [21–23].

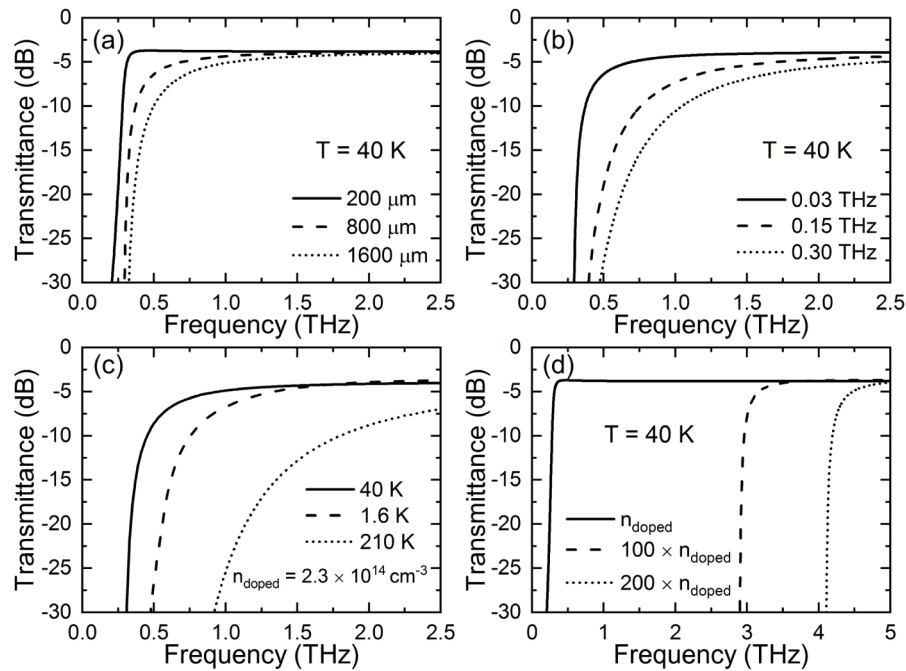


Fig. 4. Calculated THz transmittance curves for *n*-InSb samples with (a) different thicknesses ($n_{\text{doped}} = 2.3 \times 10^{14} \text{ cm}^{-3}$ and $T = 40 \text{ K}$), (b) different electron scattering rates ($n_{\text{doped}} = 2.3 \times 10^{14} \text{ cm}^{-3}$, $T = 40 \text{ K}$, and $d = 800 \mu\text{m}$), (c) different temperatures ($n_{\text{doped}} = 2.3 \times 10^{14} \text{ cm}^{-3}$ and $d = 800 \mu\text{m}$), and (d) different doping densities ($T = 40 \text{ K}$, $\nu = 0.03 \text{ THz}$, and $d = 200 \mu\text{m}$).

4. Conclusion

We investigated the THz transmission properties of a lightly *n*-doped InSb crystal and showed that it can act as a tunable THz high-pass filter through a tunable ultrasharp plasma edge with an unprecedented transmittance slope of 80 dB/THz. Through comparison with detailed theoretical calculations, we demonstrated that the edge frequency can be sensitively tuned by the temperature, electron density, scattering rate, and sample thickness. Interestingly, the edge frequency exhibited an increase with decreasing temperature below 15 K, which can be attributed to a weak-to-strong scattering transition as the temperature decreases. The plasma in InSb can also provide a controllable platform for plasma diagnostics studies since the fundamental properties of different types of plasmas such as gas discharges, space science, and near-Earth environments are remarkably similar.

Funding. National Key Research and Development Program of China (2018YFB1038603); Guiding Projects of Fujian Science and Technology Department (2019H0005).

Disclosures. The authors declare no conflicts of interest.

References

1. M. S. Dresselhaus, "Solid State Physics Part II-Optical Properties of Solids," Lecture Notes Part 2 (2001).
2. X. Wang, A. A. Belyanin, S. A. Crooker, D. M. Mittleman, and J. Kono, "Interference-induced terahertz transparency in a semiconductor magnetoplasma," *Nat. Phys.* **6**(2), 126–130 (2010).
3. T. Arikawa, X. Wang, A. A. Belyanin, and J. Kono, "Giant tunable Faraday effect in a semiconductor magneto-plasma for broadband terahertz polarization optics," *Opt. Express* **20**(17), 19484–19492 (2012).
4. P. Gogoi, D. Kamenskyi, D. D. Arslanov, R. T. Jongma, W. J. van der Zande, B. Redlich, A. F. G. van der Meer, H. Engelkamp, P. C. M. Christianen, and J. C. Maan, "Magnetoquantum oscillations at THz frequencies in InSb," *Phys. Rev. Lett.* **119**(14), 146603 (2017).

5. T. Li, F. Fan, Y. Ji, Z. Tan, Q. Mu, and S. Chang, "Terahertz tunable filter and modulator based on magneto plasmon in transverse magnetized InSb," *Opt. Lett.* **45**(1), 1–4 (2020).
6. D. Wang, B. Yang, W. Gao, H. Jia, Q. Yang, X. Chen, M. Wei, C. Liu, M. Navarro-Cia, J. Han, W. Zhang, and S. Zhang, "Photonic Weyl points due to broken time-reversal symmetry in magnetized semiconductor," *Nat. Phys.* **15**(11), 1150–1155 (2019).
7. J. Chochol, K. Postava, M. Čada, M. Vanwolleghem, L. Halagačka, D. Vignaud, J. Lampin, and J. Pištora, "Magneto-optical properties of InSb for terahertz applications," *AIP Adv.* **6**(11), 115021 (2016).
8. X. P. A. Gao, J. Y. Sohn, and S. A. Crooker, "Low temperature terahertz spectroscopy of n-InSb through a magnetic field driven metal-insulator transition," *Appl. Phys. Lett.* **89**(12), 122108 (2006).
9. Y. Lin, H. Yao, X. Ju, Y. Chen, S. Zhong, and X. Wang, "Free-standing double-layer terahertz band-pass filters fabricated by femtosecond laser micro-machining," *Opt. Express* **25**(21), 25125–25134 (2017).
10. X. Ju, D. Chen, X. Chen, T. Gao, Y. Chen, J. Wang, and X. Wang, "Significant enhancement of THz detectivity by lowering ZnTe crystal temperature in electro-optic sampling," *Opt. Mater.* **91**, 235–238 (2019).
11. E. H. Putley, "Freeze-Out Effects, Hot Electron Effects, and Submillimeter Photoconductivity in InSb," *Semicond. Semimetals* **1**, 289–313 (1966).
12. V. F. Gantmakher and Y. B. Levinson, *Carrier Scattering in Metals and Semiconductors* (Elsevier, 1987).
13. K. Seeger, *Semiconductor Physics* (Springer, 2004).
14. M. Levinstein, S. Rumyantsev, and M. Shur, *Handbook Series on Semiconductor Parameters* (World Scientific, 1996).
15. I. Vurgaftmana, J. R. Meyer, and L. R. Ram-Mohan, "Band parameters for III–V compound semiconductors and their alloys," *J. Appl. Phys.* **89**(11), 5815–5875 (2001).
16. S. Dannefaer and D. Kerr, "Positron binding energies and specific trapping rates for monovacancies in GaAs and InSb," *Phys. Rev. B* **48**(12), 9142–9145 (1993).
17. R. Pässler, "Parameter Sets Due to Fittings of the Temperature Dependencies of Fundamental Bandgaps in Semiconductors," *Phys. Status Solidi B* **216**(2), 975–1007 (1999).
18. E. D. Palik and J. K. Furdyna, "Infrared and microwave magnetoplasma effects in semiconductors," *Rep. Prog. Phys.* **33**(3), 3071193 (1970).
19. S. P. Jamison, J. Shen, D. R. Jones, R. C. Issac, B. Ersfeld, D. Clark, and D. A. Jaroszynski, "Plasma characterization with terahertz time-domain measurements," *J. Appl. Phys.* **93**(7), 4334–4336 (2003).
20. Z. Zhu, X. Zhang, J. Gu, R. Singh, Z. Tian, J. Han, and W. Zhang, "A metamaterial-based terahertz low-pass filter with low insertion loss and sharp rejection," *IEEE Trans. Terahertz Sci. Technol.* **3**(6), 832–837 (2013).
21. R. Mendis, A. Nag, F. Chen, and D. M. Mittleman, "A tunable universal terahertz filter using artificial dielectrics based on parallel-plate waveguides," *Appl. Phys. Lett.* **97**(13), 131106 (2010).
22. D. Wu, N. Fang, C. Sun, X. Zhang, W. J. Padilla, D. N. Basov, D. R. Smith, and S. Schultz, "Terahertz plasmonic high pass filter," *Appl. Phys. Lett.* **83**(1), 201–203 (2003).
23. M. Azimbeik, N. S. Badr, S. G. Zadeh, and G. Moradi, "Graphene-based high pass filter in terahertz band," *Optik* **198**, 163246 (2019).